

Theoretical design of nanocatalysts based on $(\text{Fe}_2\text{O}_3)_n$ clusters for hydrogen production from ammonia

Sapajan Ibragimov,^{1,2} Andrey Lyalin,^{3,4} Sonu Kumar,⁵ Yuriko Ono,⁵ Tetsuya Taketsugu,^{3,5} and Maciej Bobrowski²

¹*Faculty of Chemistry, Gdańsk University of Technology, Narutowi za 11/12, 80-233, Gdańsk, Poland*

²*Faculty of Technical Physics and Applied Mathematics, Gdańsk University of Technology, Narutowicza 11/12, 80-233 Gdańsk, Poland*

³*Department of Chemistry, Faculty of Science, Hokkaido University, Sapporo 060-0810, Japan*

⁴*Research Center for Energy and Environmental Materials (GREEN), National Institute for Materials Science, Namiki 1-1, Tsukuba 305-0044, Japan*

⁵*Institute for Chemical Reaction Design and Discovery (WPI-ICReDD), Hokkaido University, Sapporo 001-0021, Japan*

(*Author to whom correspondence should be addressed: lyalin@icredd.hokudai.ac.jp)

(Dated: 1 October 2024)

The catalytic activities of high-spin small Fe(III) oxides have been investigated for efficient hydrogen production through ammonia decomposition, using the Artificial Force Induced Reaction (AFIR) method within the framework of density functional theory (DFT) with the B3LYP hybrid exchange-correlation functional. Our results reveal that the adsorption free energy of NH_3 on $(\text{Fe}_2\text{O}_3)_n$ ($n = 1 - 4$) decreases with increasing cluster size up to $n = 3$, followed by a slight increase at $n = 4$. The strongest NH_3 adsorption energy, 33.68 kcal/mol, was found for Fe_2O_3 , where NH_3 interacts with a two-coordinated Fe site, forming an Fe-N bond with a length of 2.11 Å. A comparative analysis of NH_3 decomposition and H_2 formation on various Fe(III) oxide sizes identifies the rate-determining steps for each reaction. We found that the rate-determining step for the full NH_3 decomposition on $(\text{Fe}_2\text{O}_3)_n$ ($n = 1 - 4$) is size-dependent, with the $\text{NH}^* \rightleftharpoons \text{N}^* + 3\text{H}^*$ reaction acting as the limiting step for $n = 1 - 3$. Additionally, our findings indicate that H_2 formation is favored following the partial decomposition of NH_3 on Fe(III) oxides.

I. INTRODUCTION:

The ammonia decomposition reaction has recently received extensive attention due to its potential use as an alternative green energy source¹⁻⁵. One of the key advantages of ammonia as a green energy source is its ability to be liquefied at low pressure and a relatively low temperature of 20 °C, making it an attractive candidate for hydrogen storage and transportation. As with many other chemical processes, catalysts play a crucial role in ammonia decomposition to achieve fast and efficient H₂ production. Experimental and theoretical studies have demonstrated that Ru-based catalysts are the most active for ammonia decomposition⁶⁻⁸. However, ruthenium's high cost and limited availability pose challenges for its large-scale industrial application. Therefore, developing new types of cost-effective catalysts for NH₃ decomposition, based on non-noble metals or metal oxides, has become a significant area of research for effective hydrogen generation⁹. Numerous studies have focused on the activity of catalysts involving various metals and alloys¹⁰. Among the most studied non-noble metals, iron (Fe) stands out as a leading catalyst due to its low cost and availability. While the reactivity of Fe is lower compared to other transition metals, it can be enhanced by using nanoparticles instead of extended surfaces. Indeed, it is well known that the reactivity of small-size clusters can be finely tuned by adjusting their size, geometry, and electronic structure, making them promising catalysts in various catalytic processes¹¹⁻¹⁵. For example, Nishimaki, et al.¹⁶ experimentally studied ammonia decomposition on Fe nanoparticles of various grain sizes (20 nm to 1 μm) in an ammonia steam environment. Their findings indicated that the highly reactive surface of nanoparticles enhances NH₃ dissociation without increasing the nitrogen content in the gas phase, resulting in nitride phases that depend on the grain size and morphology.

As an alternative approach, ammonia decomposition reactions on small nanosized Fe clusters are frequently investigated using density functional theory (DFT) methods. Theoretical studies suggest that the mechanisms of ammonia decomposition involve stepwise dehydrogenation, where the rate-limiting step can vary depending on the size, type, and shape of the catalysts. Thus, G. Lanzani and K. Laasonen employed spin-polarized DFT to examine the adsorption and dissociation of NH₃ on a single nanosized icosahedral Fe₅₅ cluster¹⁷. Their research indicated that the overall reaction barrier for stepwise dehydrogenation was 1.48 eV, with different active sites on the Fe₅₅ cluster (facets and vertices), where the rate-limiting step was the initial hydrogen dissociation. Similarly, G.S. Otero et al.¹⁸ conducted a comprehensive comparative study on various

sizes of Fe clusters (Fe_{16} , Fe_{22} , Fe_{32} , Fe_{59} , Fe_{80} , Fe_{113} , Fe_{190}) and Fe(111) surfaces with additional adatoms. Their findings indicated that the reaction kinetics were influenced more by the strength of NH_3 adsorption rather than the activation energy barrier. Stronger NH_3 adsorption led to enhanced dissociation compared to desorption. The studies mentioned above primarily focus on the catalytic activities of large Fe clusters and Fe surfaces in the ammonia decomposition reaction. However, Xilin Zhang et al.¹⁹ specifically investigated the activities of relatively small Fe clusters, ranging from single Fe atoms to Fe_4 clusters. They found that the highest catalytic activity for stepwise NH_3 dehydrogenation was observed with nonatomic iron clusters. Interestingly, they observed that the rate-limiting steps differed: co-adsorbate NH dissociation for Fe and Fe_3 , and co-adsorbate NH_2 dissociation for Fe_2 and Fe_4 .

The NH_3 decomposition reaction can be enhanced in the presence of oxygen, where it can proceed through various pathways, including ammonia oxidation and hydrogen evolution reactions. Moreover, metal oxides are commonly employed as catalyst supports in ammonia decomposition to enhance dispersion and catalytic stability. Among these supports, widely used materials include Al_2O_3 , TiO_2 , as well as carbon nanotubes and nanofibers^{7,20–24}. However, metal oxides not only serve as support but also play a crucial role in hydrogen evolution reactions in electrocatalysis, where the oxidation state of metals significantly influences the catalytic activity of ammonia decomposition. In particular, iron-based oxides, such as Fe_2O_3 , are extensively studied forms of iron oxide due to their low cost and abundance, although their activity and stability can vary depending on their structure and size^{25–31}.

In this work, we elucidate the role of the size- and structural effects on the catalytic activity of iron-oxide-based nano-catalysts toward efficient ammonia decomposition. In particular, we investigated the theoretical mechanisms of stepwise ammonia decomposition on $(\text{Fe}_2\text{O}_3)_n$ clusters with $n = 1 - 4$ to compare the reactivity of different-sized Fe(III) oxides using the Artificial Force Induced Reaction (AFIR) method^{32,33}. Additionally, we examined the NH_3 adsorption and various energy barriers for NH_3 dehydrogenation on different active sites of Fe(III) oxides. Our investigation aims to contribute to the design of nanocatalysts based on Fe_2O_3 by exploring the activity of small-sized Fe(III) oxide clusters.

II. COMPUTATIONAL DETAILS

All calculations were performed using spin-unrestricted Kohn-Sham DFT with Becke’s three-parameter hybrid functional combined with the Lee, Yang, and Parr correlation functional, denoted as B3LYP^{34–36}. In our calculations we have employed the LANL2DZ^{37–39} basis set with effective core potentials (ECP), as well as the Pople-style 6-31+G* basis set, equivalent to 6-31+G(d), which includes polarization (d) and diffuse (sp) functions, as it is implemented in the Gaussian 16 program⁴⁰. These methods have been successfully applied to metals and metal oxide systems in previous studies. Thus, Glukhovtsev et al.⁴¹ reported that the performance of the B3LYP/ECP method for systems containing iron with various types of bonding showed good agreement with experimental data and high-level theoretical methods (CCSD(T), MCPE, CASSCF). Similarly, Taguchi, et al.⁴² studied $\text{Fe}_6\text{O}_2(\text{NO}_3)_4(\text{hmp})_8(\text{H}_2\text{O})_{22}$, $[\text{Fe}_4(\text{N}_3)_6(\text{hmp})_6]$, and $\text{Fe}_8\text{O}_3(\text{OMe})(\text{pdm})_4(\text{pdmH})_4(\text{MeOH})_{25}$ clusters using the B3LYP/LANL2DZ level of theory, obtaining results that were consistent with experimental data.

At the initial stage, the most stable isomers of iron trioxide for each selected size were investigated using the DFT method. A single iron trioxide molecule contains two Fe^{3+} ions; therefore, there are often several energetically accessible spin states (0, 1, 2, 3, 4, 5). For the starting cluster Fe_2O_3 , the lowest energy structure corresponds to the nonet state with a total spin $S=4$. For $(\text{Fe}_2\text{O}_3)_2$, the lowest energy solution was found with a total spin $S=10$, indicating an increase in the number of Fe^{3+} ions, which raises the total spin projection. For $(\text{Fe}_2\text{O}_3)_3$, the lowest energy structure was found with a total spin $S=15$, and lastly, in the case of $(\text{Fe}_2\text{O}_3)_4$, the lowest energy structure had a total spin $S=20$. Therefore, all clusters considered in our study were in a ferromagnetic configuration. We confirmed that spin contamination in the low-lying energy structures was negligible.

To analyze the most favorable pathways of NH_3 dehydrogenation and H_2 formation reactions catalyzed by small $(\text{Fe}_2\text{O}_3)_n$ ($n = 1 - 4$) clusters, we applied the SC-AFIR and DS-AFIR methods implemented in the Global Reaction Route Mapping (GRRM) strategy^{32,43–46}. These automated reaction path search methods have been successfully applied to many catalytic reactions in combination with DFT methods^{33,47–50}. The basic idea in the AFIR strategy is to push fragments (reactants) A and B of the whole system together or pull them apart by minimizing the following AFIR function³²:

$$F(Q) = E(Q) + \alpha \frac{\sum_{i \in A} \sum_{j \in B} \omega_{ij} r_{ij}}{\sum_{i \in A} \sum_{j \in B} \omega_{ij}} \quad (1)$$

The external force term in (1) perturbs the given adiabatic Potential Energy Surface (PES), $E(Q)$, with geometrical parameters Q in the AFIR function. Here, α defines the strength of the artificial force which depends on the weighted sum of the interatomic distances r_{ij} between atoms i and j , with the weights ω_{ij} defined as

$$\omega_{ij} = \left[\frac{R_i + R_j}{r_{ij}} \right]^6, \quad (2)$$

where R_i and R_j the covalent radii of atoms i and j , respectively. The force parameter α in (1) can be expressed as follows:

$$\alpha = \frac{\gamma}{\left[2^{-1/6} - (1 + \sqrt{1 + \gamma/\epsilon})^{-1/6} \right] R_0}, \quad (3)$$

where R_0 and ϵ are parameters corresponding to interatomic Lennard-Jones potentials, and parameter γ has a physical meaning of a collision energy.

This perturbation of the PES facilitates the exploration of additional approximate transition states and local minima on the surface. The model collision energy parameter γ in (3) serves as an approximate upper limit for the barrier height that the system can be affected by the AFIR function³². In our calculations, γ was set to 300 kJ/mol for the entire system. During the initial reaction path search, the LANL2DZ basis set was applied with an artificial force to yield approximate products and transition states (TS). Subsequently, we utilized the 6-31+G* basis set to optimize these approximate transition states and local minima without the artificial force, employing the Locally Updated Planes (LUP) method. The vibrational frequency calculations have been performed to confirm the nature of the stationary points, whether they are minima or transition states. The results presented in this paper include reaction route mapping at the B3LYP/LANL2DZ level and reaction pathways at the B3LYP/6-31+G(d) level.

The binding energy E_b per unit n of a $(\text{Fe}_2\text{O}_3)_n$ cluster is defined as follows:

$$E_b = - \frac{E_{\text{el}}((\text{Fe}_2\text{O}_3)_n) + E_{\text{ZPE}}((\text{Fe}_2\text{O}_3)_n) - [2nE(\text{Fe}) + 3nE(\text{O})]}{n} \quad (4)$$

where $E_{\text{el}}((\text{Fe}_2\text{O}_3)_n)$ and $E_{\text{ZPE}}((\text{Fe}_2\text{O}_3)_n)$ are the electronic and zero-point energies of a cluster $(\text{Fe}_2\text{O}_3)_n$ with a number of units n , while $E(\text{Fe})$ and $E(\text{O})$ are the energies of free Fe and O atoms.

The standard free energy of adsorption, ΔG_{ads} , is given as

$$\Delta G_{\text{ads}} = G(\text{NH}_3 @ (\text{Fe}_2\text{O}_3)_n) - (G((\text{Fe}_2\text{O}_3)_n) + G(\text{NH}_3)) \quad (5)$$

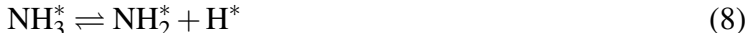
where $G(\text{NH}_3@(\text{Fe}_2\text{O}_3)_n)$ is the free energy of the most stable structure of the $(\text{Fe}_2\text{O}_3)_n$ cluster with the adsorbed ammonia molecule, $G(\text{Fe}_2\text{O}_3)_n$ is the free energy of the bare $(\text{Fe}_2\text{O}_3)_n$ cluster, and $G(\text{NH}_3)$ is the free energy of a single ammonia molecule. The values of free energy G in (5) can be calculated as follows:

$$G = E_{\text{el}} + E_{\text{ZPE}} - TS, \quad (6)$$

where E_{el} and E_{ZPE} are the electronic and zero-point energies of the system, S is the entropy of the system, and T is the temperature.

III. RESULTS AND DISCUSSION

In the present work we systematically investigated the ammonia decomposition reaction mechanisms on $(\text{Fe}_2\text{O}_3)_n$ clusters of various sizes n , where $n = 1 - 4$. Firstly, we identified approximate reaction pathways for the interactions between NH_3 molecules and the most stable isomers of $(\text{Fe}_2\text{O}_3)_n$ clusters using the AFIR technique. The obtained AFIR pathways were subsequently re-optimized along the minimum energy path using the Locally Updated Plane (LUP) method, without applying artificial forces. We calculated various reaction mechanisms and the stepwise dissociation⁵¹ of hydrogen atoms from nitrogen-containing compounds on Fe(III) oxide clusters, following the elementary steps:



Here $*$ denotes the adsorbed intermediates on the $(\text{Fe}_2\text{O}_3)_n$ cluster's surface. Finally, the adsorbed hydrogen atoms on the $(\text{Fe}_2\text{O}_3)_n$ clusters can combine to produce molecular hydrogen (H_2):





The paper is organized as follows. We first discuss the structures of free clusters, followed by the adsorption of NH_3 on the most stable isomers of $(\text{Fe}_2\text{O}_3)_n$, $n = 1 - 4$, clusters. We then examine the complete dehydrogenation and H_2 formation processes for each cluster size.

A. Structure of $(\text{Fe}_2\text{O}_3)_n$ clusters with $n = 1 - 4$

Figure 1 demonstrates the most stable structures of small $(\text{Fe}_2\text{O}_3)_n$ clusters with $n = 1 - 4$, as obtained in the present work using automated GRRM approach. A total of up to 60 isomer structures have been obtained for each cluster size n . The low-energy isomers for each cluster size, along with their relative binding energies are presented in Figs. S1-S4. The most stable structures are consistent with those obtained in our previous DFT study, which employed B3LYP functional and five different types of basis sets (LANL2DZ, 6-31+G*, 6-311+G*, Sapporo-DZP, and aug-cc-pVTZ).⁵² We found that the most stable structure of the smallest Fe_2O_3 cluster is a nonet kite-like type with a binding energy $E_b=362.7$ kcal/mol. The kite-like structure is a commonly studied configuration^{53,54} and was previously investigated by Sierka et al.⁵⁵, who observed the most stable spin configuration for this structure to be $S=0$. In contrast, we found that the lowest energy structure corresponds to a nonet state with $S=4$, while the singlet kite-like structure is 0.62 kcal/mol less stable as shown in Table S1. The results of our calculations show that the absolute binding energy of $(\text{Fe}_2\text{O}_3)_n$ rapidly increases with increasing cluster size n from 1 to 2 by 60.4 kcal/mol. However, further growth in binding energy with cluster size slows down, demonstrating a tendency for saturation as n increases.

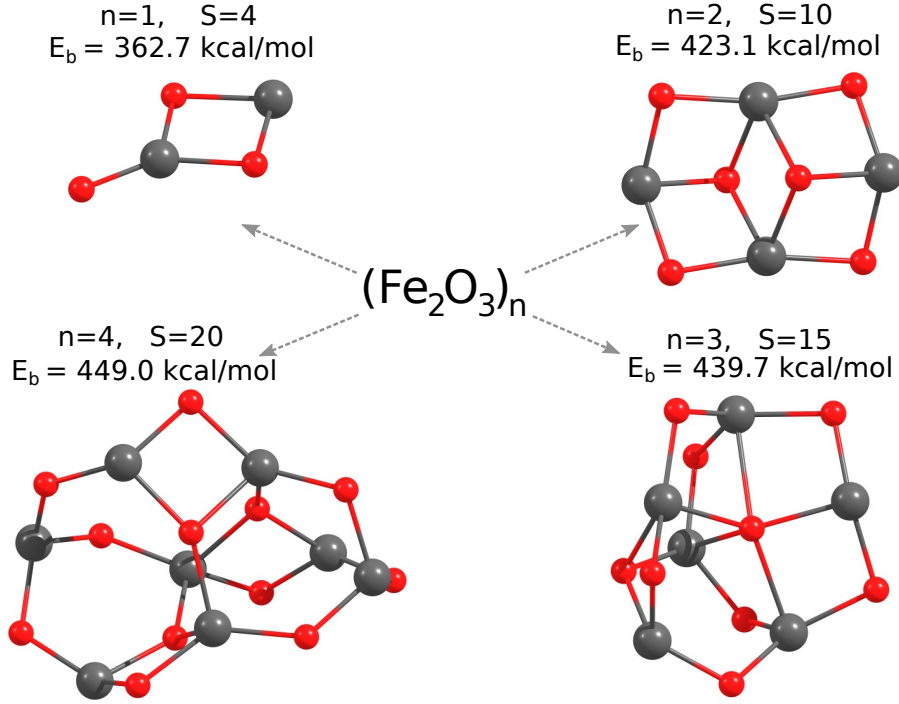


FIG. 1: The most stable structures of $(\text{Fe}_2\text{O}_3)_n$ clusters with $n = 1 - 4$. The total spin S and the binding energy E_b , of the clusters are shown in inserts.

B. Ammonia adsorption on $(\text{Fe}_2\text{O}_3)_n$ clusters

Adsorption of ammonia on $(\text{Fe}_2\text{O}_3)_n$ clusters is a crucial initial step in the whole dehydrogenation process. Figure 2 demonstrates the most stable adsorption configurations of the NH_3 molecule on $(\text{Fe}_2\text{O}_3)_n$ clusters with $n = 1 - 4$. The corresponding free energies of adsorption and Fe–N bond distances are shown in Table I at 0 K. Our calculations show that the adsorption of NH_3 on the smallest Fe_2O_3 cluster is the most stable among all cluster sizes considered in this study, with an adsorption free energy of -33.68 kcal/mol. This finding is corroborated by Mulliken charge analysis, which shows that more electrons are shared between the lone pair of the N atom and the 3d orbitals of Fe^{2+} for $n = 1$. On the other hand, for larger cluster sizes with $n = 2 - 4$, which primarily contain Fe^{3+} , the electron density is more localized over the bonding region, as also reported by Sierka et al.⁵⁵. Therefore, bonding occurs with the nitrogen lone pair.

Our theoretical analysis indicates that the adsorption energy ΔG_{ads} of ammonia on $(\text{Fe}_2\text{O}_3)_n$ clusters decreases from $n = 1$ to $n = 3$, followed by a slight increase for $n = 4$. A similar trend in the change of adsorption energy with cluster size was reported by Shulan Zhou et al.⁵⁶ for $\text{Ru}_n@\text{CNT}$ systems. We also compared the adsorption energy of NH_3 on different metal and metal oxides in

Table I. The obtained NH_3 adsorption energies on $(\text{Fe}_2\text{O}_3)_n$ clusters are about 10 kcal/mol higher than the data reported by Zhang et al. for the $\text{Ru}(0001)$ surface⁵⁷. Moreover, the adsorption of NH_3 and NO_x on the $\gamma\text{-Fe}_2\text{O}_3(111)$ surface was studied by Wei Huang et al.⁵⁸ using periodic density functional calculations. They calculated adsorption energies on octahedral and tetrahedral sites of $\gamma\text{-Fe}_2\text{O}_3(111)$ to be -2.13 kcal/mol and -21.68 kcal/mol, respectively. Similarly, our calculated NH_3 adsorption energies on $(\text{Fe}_2\text{O}_3)_n$ clusters for $n = 3$ and $n = 4$ are close to the data reported by Wei Huang et al.,⁵⁸ as adsorption of NH_3 on the three-coordinated Fe^{3+} site resembles the tetrahedral site of $\gamma\text{-Fe}_2\text{O}_3(111)$, while the adsorption on the four-coordinated Fe^{3+} site resembles the octahedral site of $\gamma\text{-Fe}_2\text{O}_3$.

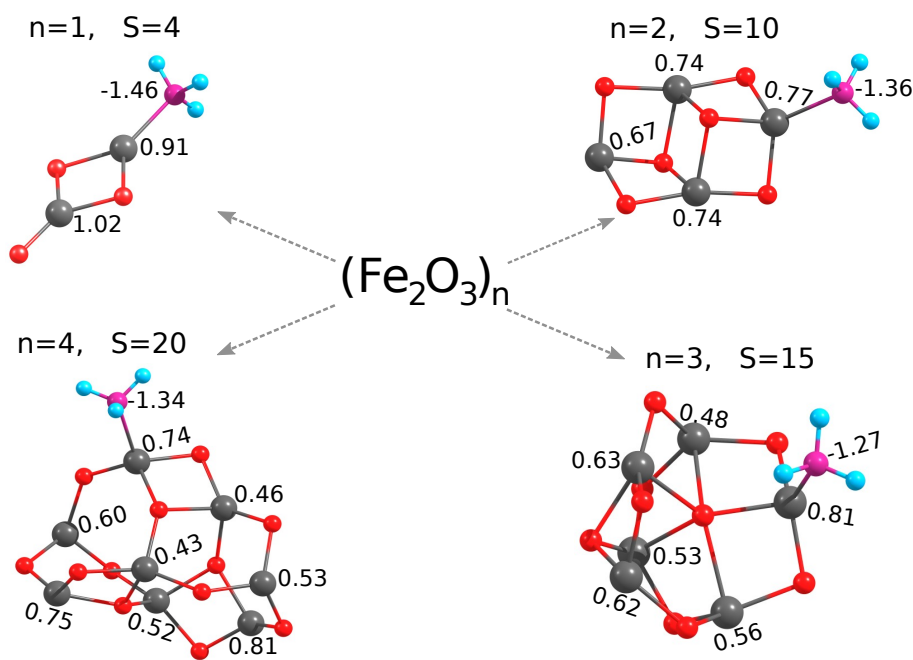


FIG. 2: The optimized geometries of NH_3 on $(\text{Fe}_2\text{O}_3)_n$ for $n = 1 - 4$; N-Fe distances (Å) are shown in parentheses along with the partial atomic charges on neighboring atoms. The total spin S of the clusters is shown in inserts.

TABLE I: NH₃ adsorption free energy ΔG_{ads} and d(Fe – N) bond length in various size of (Fe₂O₃)_n where $n = 1 - 4$.

	ΔG_{ads} (kcal/mol)	Fe – N (Å)	reference
NH ₃ /(Fe ₂ O ₃) ₁	-33.68	2.11	
NH ₃ /(Fe ₂ O ₃) ₂	-30.97	2.14	this work
NH ₃ /(Fe ₂ O ₃) ₃	-30.36	2.15	
NH ₃ /(Fe ₂ O ₃) ₄	-30.59	2.14	
NH ₃ /ZnFe ₂ O ₄ (110)	-48.54	Zn – N (2.03)	a
	-41.52	Fe – N (1.99)	
NH ₃ /Ru(0001)	-20.52	Ru – N (2.17)	b
NH ₃ /Fe ₂ O ₃ /AC	-49.12, -37.35	-	c
	-26.29, -31.13	-	
NH ₃ /γ-Fe ₂ O ₃ nano	-37.52	-	d
NH ₃ /γ-Fe ₂ O ₃ (111)	-21.68	Fe _{tet} – N (2.13)	f
	-2.13	Fe _{oct} – N (2.101)	

a⁵⁹, b⁵⁷, c⁶⁰, d⁶¹, f⁵⁸

As mentioned above, the calculated adsorption energies indicate that the adsorption of an NH₃ molecule on (Fe₂O₃)_n clusters ($n = 1 - 4$) weakens as the cluster size increases from $n = 1$ to $n = 3$. In industrial processes, the dehydrogenation of ammonia typically occurs at high temperatures, often in the range of 400°C to 700°C, depending on the specific catalysts and conditions used. Therefore, it is important to determine the range of temperatures at which ammonia adsorption on (Fe₂O₃)_n remains stable. Figure S5 demonstrates the temperature dependence of ΔG_{ads} in the range from 0 K to 1200 K for the most stable adsorption configurations of NH₃ on (Fe₂O₃)_n clusters ($n = 1 - 4$). The negative values of ΔG_{ads} correspond to stable adsorption. As seen in Fig. S5, NH₃ adsorbed on the smallest Fe₂O₃ cluster is stable across the entire temperature range of 0 K to 1200 K. However, for larger cluster sizes, ammonia adsorption becomes energetically unfavorable at temperatures of 1107 (K), 961 (K), and 1000 (K) for $n = 2, 3$, and 4, respectively.

C. NH_3 decomposition on Fe_2O_3

In this section, we discuss the complete NH_3 decomposition and H_2 formation reactions (7) - (12) on the smallest considered cluster, Fe_2O_3 , at room temperature, $T=298.15$ K, explored by the AFIR method. This method allows for the automatic exploration of the full reaction path network, systematically accounting for the variety of possible isomer structures and adsorption sites. This is an important approach in nanocatalysis because it has been demonstrated that the most stable structures are not always the most reactive. Therefore, a systematic search for reaction pathways that accounts for the contributions of low-energy isomers is required to accurately describe the catalytic properties of clusters at finite temperatures.⁴⁹

To illustrate the isomer and reaction-site effects, we explicitly consider two different isomers of the Fe_2O_3 cluster: the most stable kite-like structure with one terminal oxygen atom, and the linear structure isomer with two terminal oxygen atoms which is 6.24 kcal/mol less stable (see Fig. S1). The kite-like structure possess two type of catalytically active metal centers - two-coordinated and three-coordinated Fe sites. Therefore we consider adsorption and decomposition of NH_3 molecule on both of them.

Figure 3(a) demonstrates that the adsorption of NH_3 on the kite-like Fe_2O_3 cluster is an exothermic reaction, occurring at both the two-coordinated and three-coordinated Fe sites. The adsorption free energies are -26.98 kcal/mol for the two-coordinated Fe site (intermediate I'_11) and -11.29 kcal/mol for the three-coordinated Fe site (intermediate I''_11), respectively. The optimized structures of all intermediates (I) and transition states (T) along the reaction pathways are shown in Fig. 3(b) and 4(b), for the kite-like and linear clusters, respectively. Here the lower index corresponds to the cluster size n , while the numbering corresponds to the order of intermediates (transition states) along the reaction path. As discussed in the previous section, the most stable adsorption site for NH_3 is the two-coordinated Fe site, with an Fe–N bond length of 2.11 Å. In contrast, the Fe–N bond length at the three-coordinated Fe site is 2.16 Å. These findings are supported by the fact that NH_3 adsorption highly depends on the local geometry and electronic structure of the catalyst.

In the case of the Fe_2O_3 kite-like structure, the first dehydrogenation reaction is the second step in the reaction mechanism, occurring after adsorption with activation barriers of 26.98 kcal/mol and 22.12 kcal/mol through the reaction paths $I'_11\text{-}T'_11\text{-}I'_12$ and $I''_11\text{-}T''_11\text{-}I''_12$, respectively. The reactions on these two-coordinated and three-coordinated active sites are exothermic by 16.31

kcal/mol and 7.53 kcal/mol, respectively. However, the first dehydrogenation of NH_3 on the linear-type structure Fig. 4(a) occurs with smaller activation barrier of 16.22 kcal/mol via the reaction path $I_1^L1 - T_1^L1 - I_1^L2$, demonstrating that the less stable linear isomer is more reactive.

The role of Fe_2O_3 isomer structure on NH_3 adsorption and first hydrogen atom transfer was previously studied by Chaoyue Xie et al.⁶⁰ They performed DFT-D3 calculations on the adsorption mechanisms of different molecules (NH_3 , NO , O_2) on activated carbon (AC) supported iron-based catalysts $\text{Fe}_x\text{O}_y/\text{AC}$. The calculated adsorption electronic energies of NH_3 were -37.4 kcal/mol and -53.7 kcal/mol on different isomers of $\text{Fe}_2\text{O}_3/\text{AC}$, and the first hydrogen atom transfer had an activation barrier of 15.5 kcal/mol. Similarly, the adsorption and dehydrogenation of ammonia on different metal oxides were investigated by Erdtman and co-workers⁶² for the application of gas sensors. They reported that the adsorption energy of NH_3 on the $\text{RuO}_2(110)$ surface is -38.24 kcal/mol, and the first N–H bond cleavage had an activation energy barrier of 17.45 kcal/mol.

The third step of the NH_3 dehydrogenation reaction (9) involves the dissociation of the adsorbed NH_2^* intermediate into NH^* and H^* species. In this step, the abstracted hydrogen atom transfers to one of the oxygen atoms in the cluster. Figure 3(a) demonstrates, that in the case of the kite-like structure the energy barriers for this step are 43.91 kcal/mol and 34.51 kcal/mol, corresponding to the reaction paths $I_1'2 - T_1'2 - I_1'3$ and $I_1''2 - T_1''2 - I_1''3$, respectively.

In the fourth step (10), the adsorbed NH^* intermediate further dissociates into N^* and H^* species as shown in Fig. 3(a). The reaction barriers associated with this step are 46.98 kcal/mol and 8.95 kcal/mol for the two-coordinated and three-coordinated reaction paths, respectively. The decomposition of NH_3 on kite-like structures becomes endothermic starting from the third step (9). Our calculations reveal that NH_3 dehydrogenation has a high energy barrier when the NH_3 molecule is adsorbed at a two-coordinated Fe site, which is the most stable adsorption site. On the other hand, dehydrogenation of the adsorbed NH_3 at a three-coordinated Fe site has a considerably lower activation barrier of 8.95 kcal/mol for the reaction step (10).

Overall, for the NH_3 decomposition reaction on the kite-like Fe_2O_3 structure, with initial NH_3 adsorption on the two-coordinated Fe atom, the rate-limiting step is the fourth reaction (10), with a barrier of 46.98 kcal/mol. Alternatively, for the less favorable NH_3 adsorption on the three-coordinated Fe atom, the rate-limiting step is the third reaction step (9), with a barrier of 34.51 kcal/mol.

The reaction pathway calculated for NH_3 decomposition on the linear-type Fe_2O_3 isomer is shown in Fig. 4(a), and respective intermediate and transition state structures are shown in

Fig. 4(b). Since this structure consists of two iron atoms connected through a central oxygen, each containing a terminal oxygen, the reaction mechanism differs slightly from that of the kite-like isomer. For instance, in the third step of the reaction, the second hydrogen from the adsorbed NH_2^* intermediate is transferred to the second terminal oxygen. The energy barrier for this step on the linear-type structure is 23.8 kcal/mol, as shown in the reaction path ($I_1^L2 - T_1^L2 - I_1^L3$) in Fig. 4a.

The fourth step on this isomer is not straightforward, involving the central oxygen atom breaking its bond with one of the neighboring iron atoms while forming an Fe – N – Fe bridge. This process leads to two different intermediates: the formation of the adsorbed H_2O^* and the transfer of a hydrogen atom from one side of the Fe – N – Fe bridge to the other. Subsequently, the final dehydrogenation step from the NH^* intermediate occurs, with an activation energy barrier of 34.76 kcal/mol.

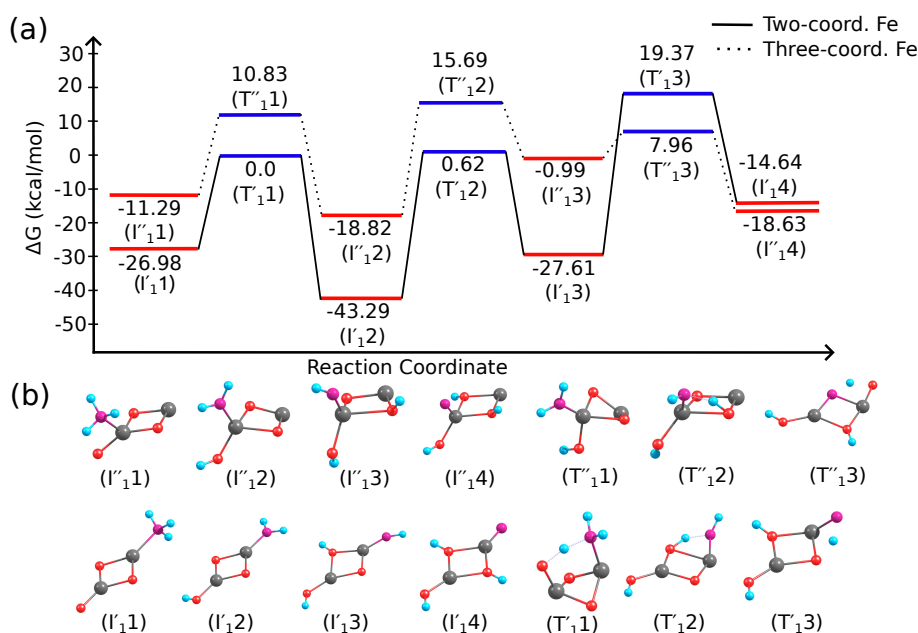


FIG. 3: (a) The energy profile for $\text{NH}_3^* \rightarrow \text{NH}_2^* + \text{H}^* \rightarrow \text{NH}^* + 2\text{H}^* \rightarrow \text{N}^* + 3\text{H}^*$ reaction path on the kite-like isomer of Fe_2O_3 at $T=298.15$ K. (b) Geometries of the optimized equilibrium and transition states along the reaction path.

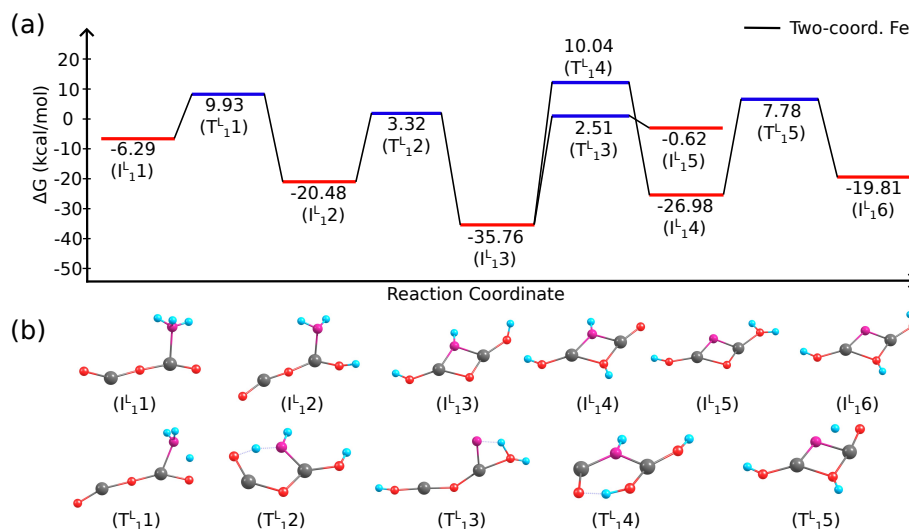


FIG. 4: (a) The energy profile for $\text{NH}_3^* \rightarrow \text{NH}_2^* + \text{H}^* \rightarrow \text{NH}^* + 2\text{H}^* \rightarrow \text{N}^* + 3\text{H}^*$ reaction path on the linear-type isomer of Fe_2O_3 at $T=298.15$ K. (b) Geometries of the optimized equilibrium and transition states along the reaction path.

As a next step we consider possible H_2 formation via reactions (11) and (12) on the kite-like and linear isomers of Fe_2O_3 cluster. The possible pathways for H_2 formation in the case of the most stable ammonia adsorption on the two-coordinated site (I' intermediates) of the kite-like Fe_2O_3 isomer are shown in Fig. 5(a), while the corresponding structures of the optimized equilibrium and transition states along the reaction path are illustrated in Fig. 5(b).

Note that H_2 formation can occur after partial decomposition of ammonia in reaction (11), starting from intermediate (I'_13) via the path $I'_13 - T'_16 - I'_17 - T'_17 - I'_18$. On the other hand, H_2 formation can occur via full decomposition of ammonia in reaction (12), through the intermediate (I'_14) via the path $I'_14 - T'_14 - I'_15 - T'_15 - I'_16$. In both cases, the reaction pathways include breaking one O–H bond and forming an Fe–H bond. The H_2 formation barriers through these intermediates are 89.74 kcal/mol and 92.49 kcal/mol, respectively. From these results, we conclude that H_2 formation on the kite-like Fe_2O_3 structure is more favorable via reaction (11), with the NH^* intermediate remaining adsorbed on the cluster. The H_2 formation reaction, starting from (I'_14), is the rate-limiting step in molecular hydrogen formation on the kite Fe_2O_3 cluster.

Similarly, the H_2 formation reaction pathways on the linear-type structure of Fe_2O_3 are shown in Fig. 6(a), while the optimized equilibrium and transition states along the reaction path are illustrated in Fig. 6(b). The H_2 formation through the NH^* intermediate (I^L_4) via the reaction path $I^L_4 - T^L_8 - I^L_9 - T^L_9 - I^L_{10}$ has an energy barrier of 79.99 kcal/mol. On the other hand H_2 formation through intermediate (I^L_6) via reaction path $I^L_6 - T^L_6 - I^L_7 - T^L_7 - I^L_8$ has an activation energy of 70.84 kcal/mol, which is about 10 kcal/mol lower energy than reaction path through

intermediate (I_1^L4).

Overall, on the basis of our calculated reaction pathways for H_2 formation show similar pattern for both kite-type and linear-type Fe_2O_3 , where H_2 formation in reactions (11) and (12) take place via breaking one of O–H bond and forming intermediate Fe–H bond. However, from both thermodynamic and kinetic perspectives, H_2 formation on the two types of Fe_2O_3 structures varies. Reaction (11) is more favorable on the kite-like structure, while reaction (12) is more favorable on the linear structure. This highlights that the rate-limiting step for H_2 formation is highly dependent on the catalyst's structure.

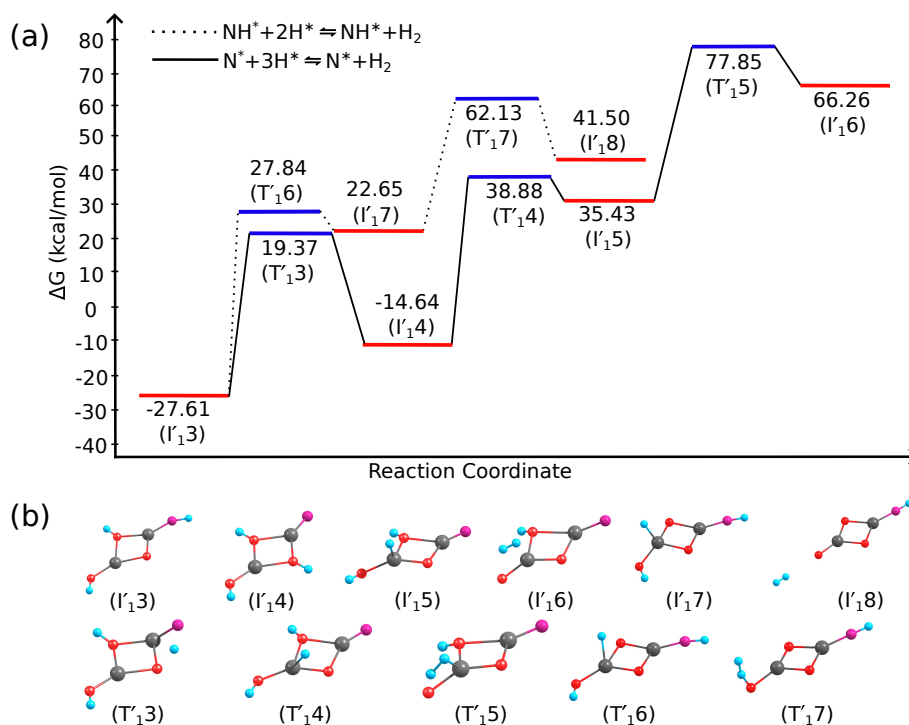


FIG. 5: (a) The energy profile for H_2 formation on the kite-like Fe_2O_3 cluster at $T=298.15$ K. (b) Geometries of the optimized equilibrium and transition states along the reaction path.

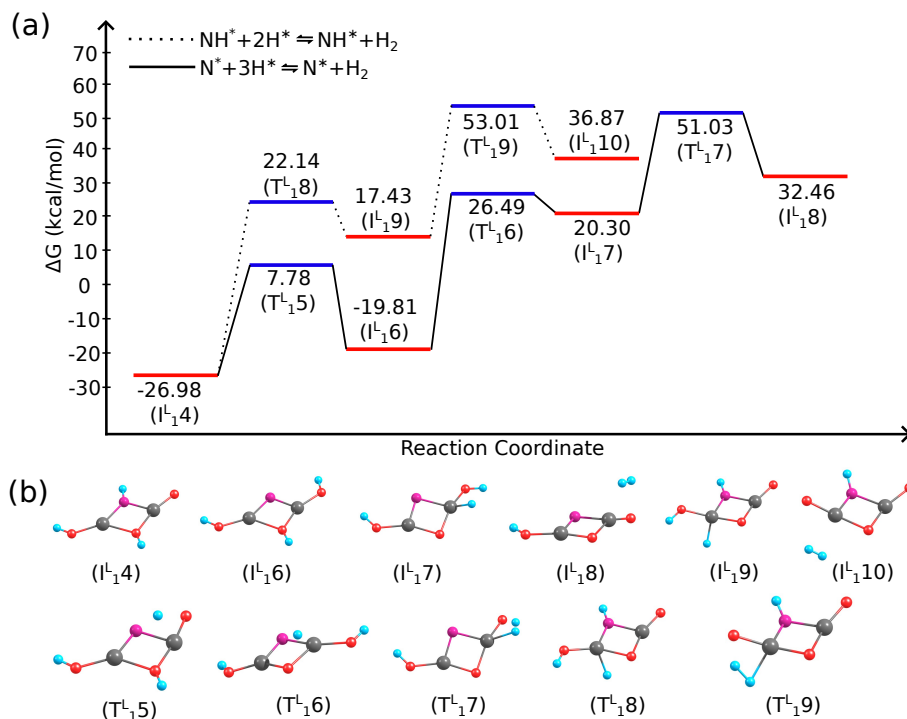


FIG. 6: (a) The energy profile for H₂ formation on the linear isomer of the Fe₂O₃ cluster at T=298.15 K. (b) Geometries of the optimized equilibrium and transition states along the reaction path.

D. NH₃ decomposition on Fe₄O₆

In the following subsection, we discuss the catalytic activity of (Fe₂O₃)₂ towards NH₃ dehydrogenation and H₂ formation reactions. On the basis of adsorption characteristics discussed in III B, the threefold coordinate Fe³⁺ site of the Fe₄O₆ cluster is the most stable site for NH₃ adsorption. Complete reaction pathway for stepwise decomposition of NH₃ and formation of H₂ reactions on (Fe₂O₃)₂ cluster are depicted in Fig. 7(a), and the corresponding intermediate and transition state structures are shown in Fig. 7(b). From this point forward, the first dehydrogenation step follows starting from the intermediate (I₂₁) where NH₃ molecule interacting with three-coordinated Fe site of (Fe₂O₃)₂ cluster by transferring a hydrogen to its one of neighboring oxygen via reaction pathway (I₂₁ - T₁₁ - I₂₂) and reaction barrier of this step is 21.47 kcal/mol which is 5.51 kcal/mol lower energy barrier than first hydrogen transfer on kite-like Fe₂O₃ cluster. This reaction also involves different isomer of (Fe₂O₃)₂, where decomposition takes place on the second minima isomer of (Fe₂O₃)₂ shown in Fig. S2. Relative binding energy of second minima isomer is 2.35 kcal/mol. The second dehydrogenation step follows from adsorbate NH₂* intermediate (I₂₂)

further dissociate to $\text{NH}^* + 2\text{H}^*$ which dissociated hydrogen atom subsequently transferred to another neighboring oxygen as shown in the reaction path (I₂₂ - T₂₂ - I₂₃). This reaction occurs with energy barrier of 38.57 kcal/mol. The ultimate dehydrogenation step is the formation of $\text{N}^* + 3\text{H}^*$ where N is bound to the central top Fe^{3+} and all the hydrogen atoms interact with three neighboring oxygens. The last dehydrogenation step occurs with the energy barrier 3.86 kcal/mol higher than the energy barrier of the second dehydrogenation step and it is shown in the reaction pathway (I₂₃ - T₂₃ - I₂₄). It suggests that dehydrogenation of adsorbate NH^* is rate-determining step on $(\text{Fe}_2\text{O}_3)_2$ cluster. Moreover, from a thermodynamic viewpoint calculated dehydrogenation steps of NH_3 on $(\text{Fe}_2\text{O}_3)_2$ cluster is endothermic by 6.24, 18.6, and 23.78 kcal/mol.

Considering H_2 formation reactions via two reaction pathways. First H_2 formation reaction (11) occurs with partial decomposition of NH_3 starting from intermediate (I₂₃) through (I₂₉). The first stage through this reaction path starting from (I₂₃), the transition state (T₂₆) was found that the H atom adsorbed on the Fe atom and formed a Fe–H bond. In the second stage of the reaction, the transition state (T₂₇) was the one that splits the adsorbed H atom from the adjacent O atom to adsorbed NH^* . Then, the dissociated H atom was adsorbed in the O atom which is an adjacent atom to the Fe–H bond, and at the final stage, the dissociative molecular H_2 formed, and barrier of this reaction is 91.1 kcal/mol.

Completed reaction pathway for reaction (11) is (I₂₃ - T₂₆ - I₂₇ - T₂₇ - I₂₈ - T₂₈ - I₂₉). The second H_2 formation reaction (12) is that occurs with fully decomposed NH_3 molecule starting from intermediate (I₂₄) through intermediate (I₂₆). It is important to note that last dehydrogenation reaction (10) is the one which has the highest barrier on the $(\text{Fe}_2\text{O}_3)_2$ cluster. So dissociative molecular hydrogen formation through this reaction path cost an energy as shown in reaction path (I₂₄ - T₂₄ - I₂₅ - T₂₅ - I₂₆). Overall, as it seen from depicted reaction pathways in Fig. 7, H_2 formation reaction is kinetically and energetically costly in reaction $\text{N}^* + 3\text{H}^* \rightleftharpoons \text{N}^* + \text{H}^* + \text{H}_2$, and it is more favorable via reaction $\text{NH}^* + 2\text{H}^* \rightleftharpoons \text{NH}^* + \text{H}_2$ which is partial decomposition of NH_3 on $(\text{Fe}_2\text{O}_3)_2$ cluster.

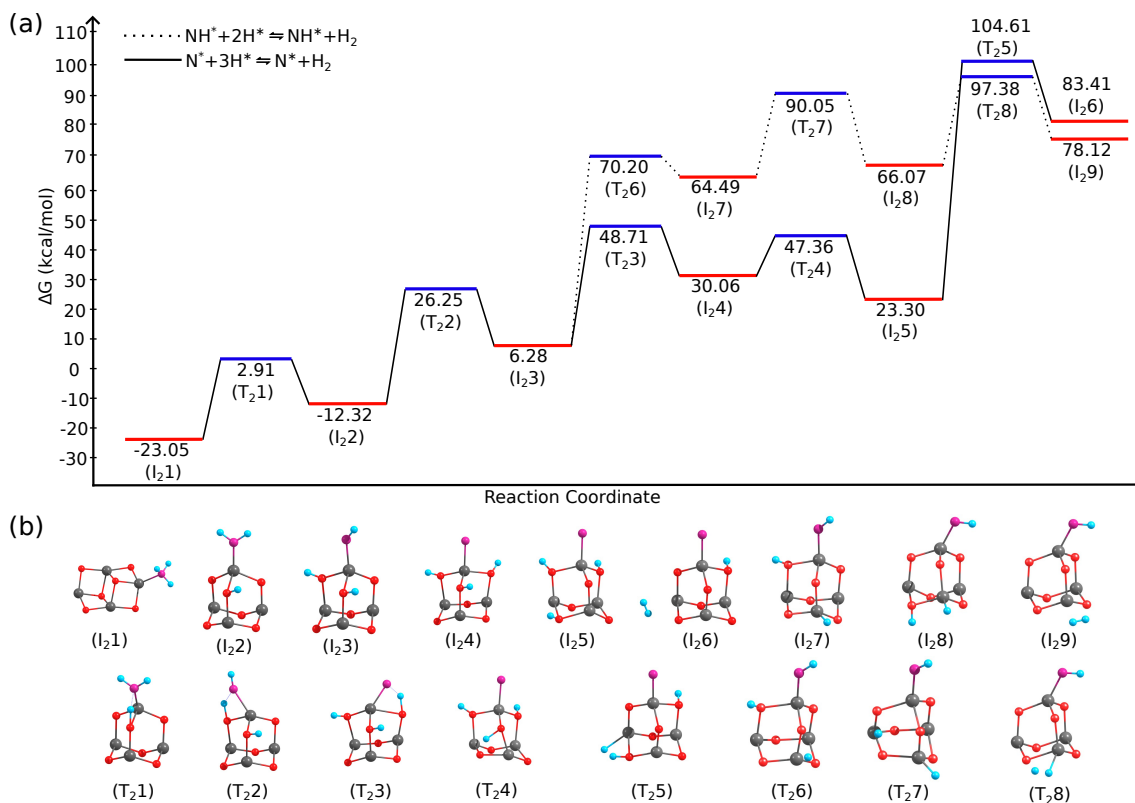


FIG. 7: (a) The energy profile for $\text{NH}_3^* \rightarrow \text{NH}_2^* + \text{H}^* \rightarrow \text{NH}^* + 2\text{H}^* \rightarrow \text{N}^* + 3\text{H}^*$ and H_2 formation reaction paths on the $(\text{Fe}_2\text{O}_3)_2$ at $T=298.15$ K. (b) Geometries of the optimized equilibrium and transition states along the reaction path.

E. NH_3 decomposition on Fe_6O_9

The energy profile for the stepwise dehydrogenation of NH_3 on the $(\text{Fe}_2\text{O}_3)_3$ cluster is presented in Fig. 8(a), while the intermediate and transition state structures along this reaction pathway are shown in Fig. 8(b). The dissociation of NH_3 on the $(\text{Fe}_2\text{O}_3)_3$ cluster is more complex compared to smaller Fe(III) oxide structures, as NH_3 can adsorb at various sites on the $(\text{Fe}_2\text{O}_3)_3$ surface.

We identified the most favorable adsorption configuration, I_31 , with an adsorption energy of $\Delta G = -21.51$ kcal/mol, from which the stepwise decomposition reaction proceeds. The first dehydrogenation reaction, as described in (8), begins with NH_3^* adsorbed on the $(\text{Fe}_2\text{O}_3)_3$ cluster as I_31 and proceeds through the transition state T_31 . The energy barrier along this pathway is 22.75 kcal/mol, which is slightly higher than the barrier for the first H abstraction from NH_3 on the $(\text{Fe}_2\text{O}_3)_2$ cluster. Although the first dehydrogenation reaction on the $(\text{Fe}_2\text{O}_3)_3$ cluster is

endothermic, we observed that when the NH_2^* species migrates to a bridging position between two Fe atoms (Fe – N – Fe), the reaction becomes exothermic by 11.44 kcal/mol, as shown in the reaction pathways $\text{I}_{32} - \text{T}_{32} - \text{I}_{33}$ and $\text{I}_{33} - \text{T}_{33} - \text{I}_{34}$.

The second H abstraction involves the further dehydrogenation of NH_2^* into NH^* and H^* , with an energy barrier of 35.97 kcal/mol along the pathway $\text{I}_{34} - \text{T}_{34} - \text{I}_{35}$. This barrier is 10 kcal/mol higher than that of the first dehydrogenation step. Additionally, this reaction is endothermic, with a reaction energy of 15.74 kcal/mol.

Similarly, in the third step (10), the remaining NH^* dissociates into N^* and H^* , with an energy barrier 17.94 kcal/mol higher than that of the second dissociation step. This is the largest barrier encountered in the decomposition of NH_3 . The calculated reaction pathway indicates that this process is endothermic, with a reaction energy of 25.76 kcal/mol.

Lastly, the possible H_2 formation reactions (11 and 12) on the $(\text{Fe}_2\text{O}_3)_3$ cluster were calculated, as shown in Fig. 8. The first H_2 formation reaction (11) begins with one adsorbed NH^* and two H^* species on the $(\text{Fe}_2\text{O}_3)_3$ cluster. The reaction proceeds in a manner similar to that discussed in the previous subsection: the adsorbed H^* on oxygen, adjacent to the NH^* adsorbed on Fe, migrates away by forming Fe–H bonds through transition states T_{37} and T_{38} . The overall energy barrier for H_2 formation via reaction (11) is 100.74 kcal/mol.

The second possible H_2 formation pathway starts from fully decomposed NH_3 (I_{36}) and proceeds through the transition state T_{36} . This pathway has a significantly high energy barrier, calculated to be 116.89 kcal/mol, as shown in the reaction path $\text{I}_{36} - \text{T}_{36} - \text{I}_{37}$. These results suggest that, from both a thermodynamic and kinetic perspective, H_2 formation after full dehydrogenation of NH_3 is less favorable.

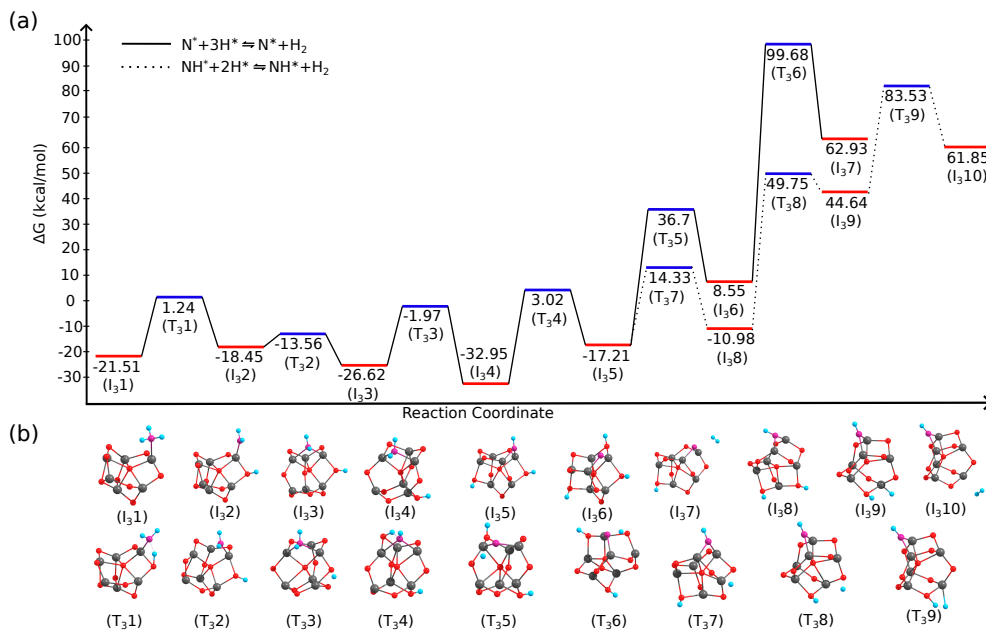


FIG. 8: (a) The energy profile for $\text{NH}_3^* \rightarrow \text{NH}_2^* + \text{H}^* \rightarrow \text{NH}^* + 2\text{H}^* \rightarrow \text{N}^* + 3\text{H}^*$ and H_2 formation reaction paths on the $(\text{Fe}_2\text{O}_3)_3$ at $T=298.15$ K. (b) Geometries of the optimized equilibrium and transition states along the reaction path.

F. NH_3 decomposition on Fe_8O_{12}

Finally, the decomposition of NH_3 and the H_2 formation pathways on the $(\text{Fe}_2\text{O}_3)_4$ cluster are illustrated in Fig. 9(a), with the intermediate and transition state structures shown in Fig. 9(b). As discussed in previous subsections, increasing the number of units n in $(\text{Fe}_2\text{O}_3)_n$ increases the number of active sites that interact with NH_3 . However, similar to the reactions on $(\text{Fe}_2\text{O}_3)_n$ ($n = 2, 3$), the most stable adsorption site for NH_3 on $(\text{Fe}_2\text{O}_3)_4$ is a three-coordinated Fe site, with an adsorption energy of -21.94 kcal/mol at room temperature, slightly higher than that on $(\text{Fe}_2\text{O}_3)_3$. The dehydrogenation of NH_3 begins with the adsorption of NH_3^* , as shown in the intermediate state I_{41} . The first dehydrogenation step involves breaking one N–H bond and forming an O–H bond, with an energy barrier of 22.48 kcal/mol, as shown in the reaction pathway $\text{I}_{41} - \text{T}_{41} - \text{I}_{42}$. The second dehydrogenation step (9) involves the dissociation of $\text{NH}_2^* + \text{H}^*$ to form $\text{NH}^* + 2\text{H}^*$, proceeding through the transition state T_{42} . The energy barrier for this step is 43.96 kcal/mol, which is higher than the corresponding second dehydrogenation steps on $(\text{Fe}_2\text{O}_3)_n$ ($n = 1 - 3$). The final dehydrogenation step occurs along the pathway $\text{I}_{43} - \text{T}_{43} - \text{I}_{44}$, with a barrier of 42.24 kcal/mol. All NH_3 dehydrogenation steps on $(\text{Fe}_2\text{O}_3)_4$ are endothermic, with reaction energies of 3.85 kcal/mol, 15.39 kcal/mol, and 41.47 kcal/mol, respectively.

The final reaction pathway on the $(\text{Fe}_2\text{O}_3)_4$ cluster involves H_2 formation from both partially and fully decomposed NH_3 , as described in (11) and (12). As observed for all sizes of $(\text{Fe}_2\text{O}_3)_n$ clusters, H_2 formation is energetically more favorable after the partial decomposition of NH_3 in reaction (11) compared to the fully decomposed pathway (12). However, this pathway also presents the highest energy barrier on this cluster.

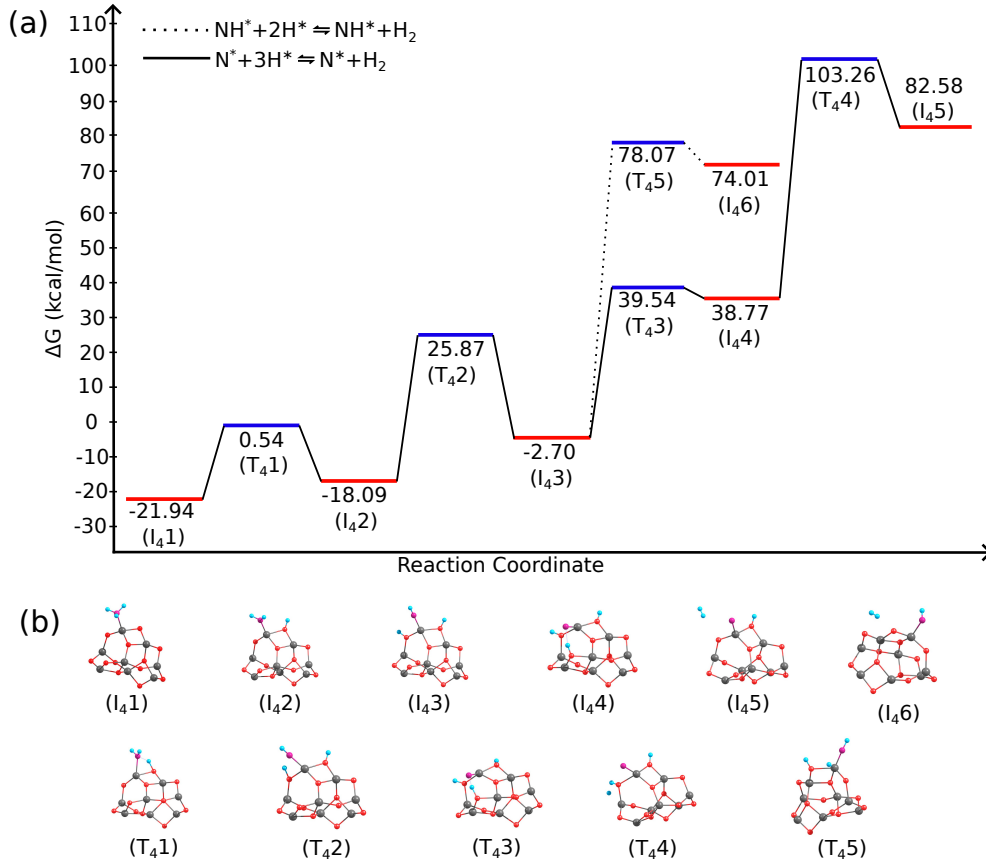


FIG. 9: (a) The energy profile for $\text{NH}_3 \rightarrow \text{NH}_2^* + \text{H}^* \rightarrow \text{NH}^* + 2\text{H}^* \rightarrow \text{N}^* + 3\text{H}^*$ and H_2 formation reaction path on the $(\text{Fe}_2\text{O}_3)_4$ at $T=298.15$ K. (b) Geometries of the optimized equilibrium and transition states along the reaction path.

IV. COMPARISON AND CONCLUSION

Our results, illustrated in Fig. 3, Fig. 4, Fig. 7, Fig. 8, and Fig. 9, indicate that NH_3 dehydrogenation can be a thermodynamically favorable reaction on $(\text{Fe}_2\text{O}_3)_n$ ($n = 1 - 4$) clusters. However, the favorability depends on the size and geometry of the cluster, as well as the specific reaction steps described in (8) – (12).

To compare the activity of various sizes and structures of $(\text{Fe}_2\text{O}_3)_n$ ($n = 1 - 4$), we have cal-

culated the change in Gibbs free energy (ΔG) as a function of temperature at 1 bar pressure, as shown in Fig. S6. Across all reactions studied, we observed that ΔG increases with temperature. This suggests that NH_3 dehydrogenation on $(\text{Fe}_2\text{O}_3)_n$ ($n = 2, 4$) can be energetically favorable at moderate temperatures, depending on the specific reaction step. However, as the temperature rises beyond a certain threshold, the reaction becomes unfavorable.

For example, as shown in Fig. S6 (a), (b), and (c), all dehydrogenation reactions on $(\text{Fe}_2\text{O}_3)_n$ ($n = 1$) are energetically favorable within the temperature range of 0–1000 K. In contrast, on $(\text{Fe}_2\text{O}_3)_n$ ($n = 2, 4$), only the last dehydrogenation step is limiting. Since the ΔG of the third dehydrogenation reaction is already greater than zero at 0 K, this step is not favorable at any temperature. Another larger cluster considered in this study, $(\text{Fe}_2\text{O}_3)_n$ ($n = 3$), exhibits better stability of the reaction intermediates during the second dehydrogenation step, remaining favorable up to 800 K. On the other hand, the second dehydrogenation reaction on $(\text{Fe}_2\text{O}_3)_n$ ($n = 4$) is favorable only up to 400 K. The most endothermic dehydrogenation reaction on this cluster is the step $\text{NH}^* \rightleftharpoons \text{N}^* + 3\text{H}^*$. The first and second dehydrogenation steps are favorable up to 1100 K and 700 K, respectively.

Moreover, we observed the variation of ΔG with temperature for the H_2 formation reaction on $(\text{Fe}_2\text{O}_3)_n$ ($n = 1 - 4$). Our results indicate that the formation of molecular hydrogen is not thermodynamically favorable at any temperature. However, temperature is not the only factor determining whether the reaction occurs. If sufficient energy is available to overcome the activation barrier, the reaction can still proceed.

The effective production of molecular hydrogen from ammonia is determined by the stepwise dehydrogenation of adsorbed ammonia on the catalyst. Catalytic reaction mechanisms are analyzed by identifying the rate-determining step in the dehydrogenation of NH_3 , which corresponds to the step requiring the highest energy to activate the N–H bond. However, it is important to note that in catalysis, the overall energy barrier is more significant than the barrier for any single intermediate reaction step.

Several studies have reported different rate-determining steps depending on the type of catalyst used⁶³. Xiuyuan Lu et al. found that the rate-determining step in NH_3 decomposition on different phases of Ru surface catalysts is the formation of molecular nitrogen⁶⁴. In contrast, studies by Xilin Zhang et al.¹⁹ on ammonia decomposition on small iron clusters showed that the rate-determining step on single Fe and Fe_3 is the $\text{NH} \rightarrow \text{N} + \text{H}$ step, whereas for Fe_2 and Fe_4 , the rate-determining step is the $\text{NH}_2 \rightarrow \text{NH} + \text{H}$ step. Similarly, a detailed comparison of the energy

barriers for each elementary step in NH_3 decomposition and H_2 formation on different sizes and shapes of $(\text{Fe}_2\text{O}_3)_n$ ($n = 1 - 4$) is shown in Fig. 10. Based on the results from our calculations, the rate-determining step in ammonia decomposition and H_2 formation varies with the size of the $(\text{Fe}_2\text{O}_3)_n$ ($n = 1 - 4$) oxide clusters. In general, the final step of H_2 formation represents the highest energy barrier on all $(\text{Fe}_2\text{O}_3)_n$ ($n = 1 - 4$) clusters. However, the analysis of NH_3 decomposition shows that the $\text{NH} \rightarrow \text{N} + \text{H}$ step is typically the rate-determining step, except in the case of $(\text{Fe}_2\text{O}_3)_4$, where the rate-determining step is the second H dissociation step. Furthermore, the first dehydrogenation step exhibits an energy barrier that is nearly identical across all clusters, with the process being exothermic for clusters $n = 1$ and $n = 3$, and endothermic for clusters $n = 2$ and $n = 4$. For the second dehydrogenation step, $(\text{Fe}_2\text{O}_3)_3$ demonstrates significantly higher activity compared to the other cluster sizes. It is also important to note that $n = 1$ (linear) is the only special configuration of Fe_2O_3 containing two terminal O^{-2} ions, unlike the other types of Fe_2O_3 , which may promote a potentially high activity for NH_3 dehydrogenation and molecular hydrogen formation. Overall, the lowest energy barrier observed for H_2 formation is associated with the largest cluster considered in this study.

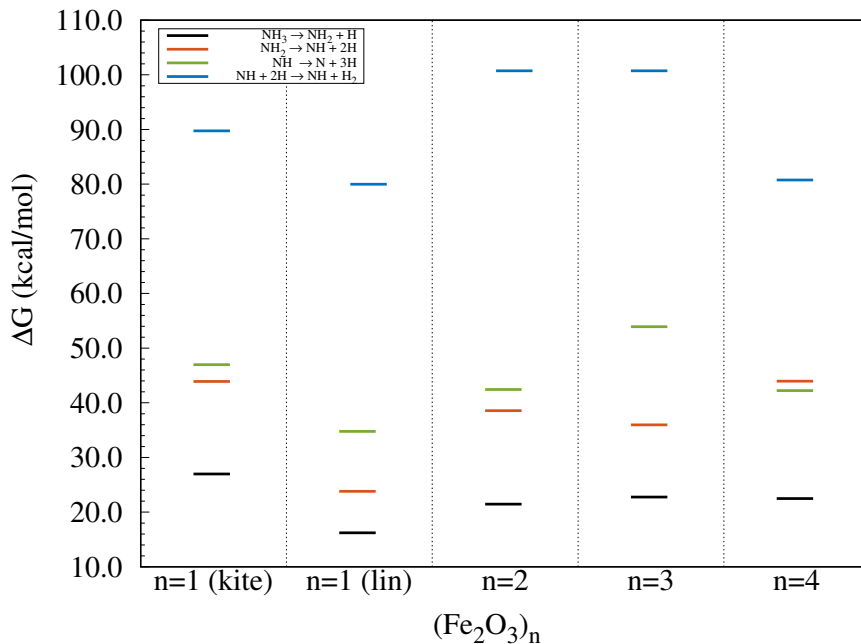


FIG. 10: Reaction barrier (ΔG^\ddagger) for NH_3 dehydrogenation and H_2 formation reactions on $(\text{Fe}_2\text{O}_3)_n$ ($n = 1 - 4$) clusters.

In this research, various structures of $(\text{Fe}_2\text{O}_3)_n$ ($n = 1 - 4$) were obtained using the SC-AFIR method, and we investigated the ammonia decomposition and molecular hydrogen formation reac-

tion pathways on the most stable isomers of $(\text{Fe}_2\text{O}_3)_n$ ($n = 1 - 4$) clusters. This analysis employed the SC-AFIR and DS-AFIR methods within the Global Reaction Route Mapping (GRRM) strategy, utilizing the B3LYP exchange-correlation functional in Kohn-Sham DFT.

The results indicate that the catalytic activity in ammonia decomposition varies depending on the size and shape of the high-spin iron trioxides. The adsorption analysis reveals that the NH_3 molecule preferentially adsorbs at two-coordinated Fe sites in $n = 1$, and at three-coordinated Fe sites in $n = 2 - 4$ clusters. Furthermore, the adsorption energy tends to decrease from $n = 1$ to $n = 3$ of the $(\text{Fe}_2\text{O}_3)_n$ clusters, then slightly increases for the $(\text{Fe}_2\text{O}_3)_4$ cluster.

From a thermodynamic perspective, the adsorption of the NH_3 molecule on $(\text{Fe}_2\text{O}_3)_1$ is favorable across the entire temperature range of 0 K to 1200 K. In contrast, for the larger clusters $(\text{Fe}_2\text{O}_3)_n$ ($n = 2, 4$), ammonia adsorption becomes energetically unfavorable at temperatures of 1107 K, 961 K, and 1000 K for $n = 2, 3$, and 4, respectively.

A comparison of the rate-determining steps in the ammonia dehydrogenation reaction reveals a dependency on the size of the iron trioxide clusters. Thus, the reaction step $\text{NH}^* \rightarrow \text{N}^* + \text{H}^*$ is the rate-determining step for the smaller iron trioxide clusters $(\text{Fe}_2\text{O}_3)_n$ ($n = 1 - 3$). In contrast, the reaction step $\text{NH}_2^* \rightarrow \text{NH}^* + \text{H}^*$ is identified as the rate-determining step for the $(\text{Fe}_2\text{O}_3)_n$ ($n = 4$) cluster. Additionally, we observed that the energy barrier for molecular hydrogen formation increases with the size of the clusters $(\text{Fe}_2\text{O}_3)_n$ ($n = 1 - 3$) but then experiences a drastic decrease for the $(\text{Fe}_2\text{O}_3)_4$ cluster.

We have investigated the catalytic activity of high-spin $(\text{Fe}_2\text{O}_3)_n$ ($n = 1 - 4$) clusters for decomposition of NH_3 . We believe that the results are valuable for designing iron trioxide-based nanosized catalysts by regulating the size of the $(\text{Fe}_2\text{O}_3)_n$ clusters to enhance H_2 production from the catalytic decomposition of ammonia.

ACKNOWLEDGMENTS

This work was partly supported by MEXT Program: Data Creation and Utilization-Type Material Research and Development Project Grant Number JPMXP1122712807, and partially supported by NAWA "STE(E)R-ING towards International Doctoral School" Calculations were performed using computational resources of the Institute for Solid State Physics, the University of Tokyo, Japan, and the Research Center for Computational Science, Okazaki, Japan (Project: 23-IMS-C016). S.I. is grateful to the MANABIYA system of the Institute for Chemical Reaction De-

sign and Discovery (ICReDD) of Hokkaido University, which was established by the World Premier International Research Initiative (WPI), MEXT, Japan, to support the learning of the GRRM program techniques for DFT calculations.

REFERENCES

- ¹D. A. Hansgen, D. G. Vlachos, and J. G. Chen, *Nature chemistry* **2**, 484 (2010).
- ²C. Plana, S. Armenise, A. Monzón, and E. García-Bordejé, *Journal of Catalysis* **275**, 228 (2010).
- ³H. Liu, H. Wang, J. Shen, Y. Sun, and Z. Liu, *Catalysis today* **131**, 444 (2008).
- ⁴R. Lan, J. T. Irvine, and S. Tao, *International journal of hydrogen energy* **37**, 1482 (2012).
- ⁵A. Klerke, C. H. Christensen, J. K. Nørskov, and T. Vegge, *Journal of Materials Chemistry* **18**, 2304 (2008).
- ⁶J. C. Ganley, F. Thomas, E. Seebauer, and R. I. Masel, *Catalysis Letters* **96**, 117 (2004).
- ⁷S.-F. Yin, Q.-H. Zhang, B.-Q. Xu, W.-X. Zhu, C.-F. Ng, and C.-T. Au, *Journal of Catalysis* **224**, 384 (2004).
- ⁸Á. Logadóttir and J. K. Nørskov, *Journal of Catalysis* **220**, 273 (2003).
- ⁹I. Lucentini, X. Garcia, X. Vendrell, and J. Llorca, *Industrial & Engineering Chemistry Research* **60**, 18560 (2021).
- ¹⁰L. Yao, T. Shi, Y. Li, J. Zhao, W. Ji, and C.-T. Au, *Catalysis Today* **164**, 112 (2011).
- ¹¹K. Zemski, D. Justes, and A. Castleman, “Studies of metal oxide clusters: Elucidating reactive sites responsible for the activity of transition metal oxide catalysts,” (2002).
- ¹²D. Yang, M. Babucci, W. H. Casey, and B. C. Gates, *ACS central science* **6**, 1523 (2020).
- ¹³E. C. Tyo and S. Vajda, *Nature nanotechnology* **10**, 577 (2015).
- ¹⁴U. Heiz and U. Landman, *Nanocatalysis* (Springer Science & Business Media, 2007).
- ¹⁵A. Fernando, K. D. M. Weerawardene, N. V. Karimova, and C. M. Aikens, *Chemical reviews* **115**, 6112 (2015).
- ¹⁶K. Nishimaki, S. Ohmae, T. Yamamoto, and M. Katsura, *Nanostructured Materials* **12**, 527 (1999).
- ¹⁷G. Lanzani and K. Laasonen, *International journal of hydrogen energy* **35**, 6571 (2010).
- ¹⁸G. S. Otero, B. Pascucci, M. M. Branda, R. Miotto, and P. G. Belelli, *Computational Materials Science* **124**, 220 (2016).
- ¹⁹X. Zhang, Z. Lu, D. Ma, and Z. Yang, *international journal of hydrogen energy* **40**, 346 (2015).

- ²⁰J. Zhang, H. Xu, X. Jin, Q. Ge, and W. Li, *Applied Catalysis A: General* **290**, 87 (2005).
- ²¹A. M. Karim, V. Prasad, G. Mpourmpakis, W. W. Lonergan, A. I. Frenkel, J. G. Chen, and D. G. Vlachos, *Journal of the American Chemical Society* **131**, 12230 (2009).
- ²²J. Ji, X. Duan, G. Qian, P. Li, X. Zhou, D. Chen, and W. Yuan, *Catalysis today* **216**, 254 (2013).
- ²³J. Zhang, M. Comotti, F. Schüth, R. Schlögl, and D. S. Su, *Chemical communications* , 1916 (2007).
- ²⁴D. Xuezhi, Z. Jinghong, Q. Gang, L. Ping, Z. Xinggui, and C. De, *Chinese Journal of Catalysis* **31**, 979 (2010).
- ²⁵Q. Yang, X.-P. Fu, C.-J. Jia, C. Ma, X. Wang, J. Zeng, R. Si, Y.-W. Zhang, and C.-H. Yan, *ACS Catalysis* **6**, 3072 (2016).
- ²⁶N. Iordanova, M. Dupuis, and K. M. Rosso, *The Journal of chemical physics* **122** (2005).
- ²⁷M. Sánchez, L. Sabio, N. Gálvez, M. Capdevila, and J. M. Dominguez-Vera, *IUBMB life* **69**, 382 (2017).
- ²⁸L. Machala, J. Tucek, and R. Zboril, *Chemistry of materials* **23**, 3255 (2011).
- ²⁹F. Yingying, W. Jie, and D. Yong, (2016).
- ³⁰Q. Shi, Y. Zhou, J. Cheng, Y. Pan, Y. Wu, L. Zhu, and Z. Yuan, *Microporous and Mesoporous Materials* **332**, 111681 (2022).
- ³¹H. Zhao, M. Jiang, Q. Kang, L. Liu, N. Zhang, P. Wang, and F. Zhou, *Catalysis Science & Technology* **10**, 8305 (2020).
- ³²S. Maeda, T. Taketsugu, and K. Morokuma, *Journal of computational chemistry* **35**, 166 (2014).
- ³³W. Sameera, A. Kumar Sharma, S. Maeda, and K. Morokuma, *The Chemical Record* **16**, 2349 (2016).
- ³⁴A. D. Becke, *J. Chem. Phys.* **98**, 5648 (1993).
- ³⁵P. J. Stephens, F. J. Devlin, C. F. Chabalowski, and M. J. Frisch, *J. Phys. Chem.* **98**, 11623 (1994).
- ³⁶R. H. Hertwig and W. Koch, *Chem. Phys. Lett.* **268**, 345 (1997).
- ³⁷P. J. Hay and W. R. Wadt, *J. Chem. Phys.* **82**, 270 (1985).
- ³⁸W. R. Wadt and P. J. Hay, *J. Chem. Phys.* **82**, 284 (1985).
- ³⁹P. J. Hay and W. R. Wadt, *J. Chem. Phys.* **82**, 299 (1985).
- ⁴⁰M. J. Frisch, G. W. Trucks, H. B. Schlegel, G. E. Scuseria, M. A. Robb, J. R. Cheeseman, G. Scalmani, V. Barone, G. A. Petersson, H. Nakatsuji, X. Li, M. Caricato, A. V. Marenich, J. Bloino, B. G. Janesko, R. Gomperts, B. Mennucci, H. P. Hratchian, J. V. Ortiz, A. F. Iz-

- maylov, J. L. Sonnenberg, D. Williams-Young, F. Ding, F. Lipparini, F. Egidi, J. Goings, B. Peng, A. Petrone, T. Henderson, D. Ranasinghe, V. G. Zakrzewski, J. Gao, N. Rega, G. Zheng, W. Liang, M. Hada, M. Ehara, K. Toyota, R. Fukuda, J. Hasegawa, M. Ishida, T. Nakajima, Y. Honda, O. Kitao, H. Nakai, T. Vreven, K. Throssell, J. A. Montgomery, Jr., J. E. Peralta, F. Ogliaro, M. J. Bearpark, J. J. Heyd, E. N. Brothers, K. N. Kudin, V. N. Staroverov, T. A. Keith, R. Kobayashi, J. Normand, K. Raghavachari, A. P. Rendell, J. C. Burant, S. S. Iyengar, J. Tomasi, M. Cossi, J. M. Millam, M. Klene, C. Adamo, R. Cammi, J. W. Ochterski, R. L. Martin, K. Morokuma, O. Farkas, J. B. Foresman, and D. J. Fox, "Gaussian 16 Revision C.01," (2016), gaussian Inc. Wallingford CT.
- ⁴¹M. N. Glukhovtsev, R. D. Bach, and C. J. Nagel, *The Journal of Physical Chemistry A* **101**, 316 (1997).
- ⁴²T. Taguchi, T. C. Stamatatos, K. A. Abboud, C. M. Jones, K. M. Poole, T. A. O'Brien, and G. Christou, *Inorganic chemistry* **47**, 4095 (2008).
- ⁴³S. Maeda and K. Morokuma, *The Journal of chemical physics* **132** (2010).
- ⁴⁴S. Maeda and K. Morokuma, *Journal of Chemical Theory and Computation* **7**, 2335 (2011).
- ⁴⁵S. Maeda, K. Ohno, and K. Morokuma, *Physical Chemistry Chemical Physics* **15**, 3683 (2013).
- ⁴⁶S. Maeda, Y. Harabuchi, M. Takagi, K. Saita, K. Suzuki, T. Ichino, Y. Sumiya, K. Sugiyama, and Y. Ono, "Implementation and performance of the artificial force induced reaction method in the grm17 program," (2018).
- ⁴⁷A. K. Sharma, W. Sameera, M. Jin, L. Adak, C. Okuzono, T. Iwamoto, M. Kato, M. Nakamura, and K. Morokuma, *Journal of the American Chemical Society* **139**, 16117 (2017).
- ⁴⁸B. B. Skjelstad, T. Helgaker, S. Maeda, and D. Balcells, *ACS Catalysis* **12**, 12326 (2022).
- ⁴⁹M. Gao, A. Lyalin, S. Maeda, and T. Taketsugu, *Journal of Chemical Theory and Computation* **10**, 1623 (2014).
- ⁵⁰M. Gao, A. Lyalin, M. Takagi, S. Maeda, and T. Taketsugu, *The Journal of Physical Chemistry C* **119**, 11120 (2015).
- ⁵¹A. Hellman, K. Honkala, I. Remediakis, A. Logadottir, A. Carlsson, S. Dahl, C. H. Christensen, and J. K. Nørskov, *Surface Science* **603**, 1731 (2009).
- ⁵²S. Ibragimov, S. Freza, I. Anusiewicz, P. Skurski, and M. Bobrowski, to be submitted.
- ⁵³H. Shiroishi, T. Oda, I. Hamada, and N. Fujima, *The European Physical Journal D-Atomic, Molecular, Optical and Plasma Physics* **24**, 85 (2003).
- ⁵⁴N. Jones, B. Reddy, F. Rasouli, and S. N. Khanna, *Physical Review B* **72**, 165411 (2005).

- ⁵⁵A. Erlebach, C. Hühn, R. Jana, and M. Sierka, *Physical Chemistry Chemical Physics* **16**, 26421 (2014).
- ⁵⁶S. Zhou, S. Lin, and H. Guo, *The Journal of Physical Chemistry C* **122**, 9091 (2018).
- ⁵⁷C. Zhang, M. Lynch, and P. Hu, *Surface science* **496**, 221 (2002).
- ⁵⁸W. Huang, L. Wang, L. Dong, H. Hu, and D. Ren, *Molecules* **28**, 2371 (2023).
- ⁵⁹C.-y. Zou, W. Ji, Z. Shen, Q. Tang, and M. Fan, *Applied Surface Science* **442**, 778 (2018).
- ⁶⁰C. Xie, Y. Sun, B. Zhu, W. Song, and M. Xu, *New Journal of Chemistry* **45**, 3169 (2021).
- ⁶¹D. Ren and K. Gui, *Applied Surface Science* **487**, 171 (2019).
- ⁶²E. Erdtman, M. Andersson, A. L. Spetz, and L. Ojamäe, *Surface Science* **656**, 77 (2017).
- ⁶³S. R. Kulkarni, N. Realpe, A. Yerrayya, V. K. Velisoju, S. Sayas, N. Morlanes, J. Cerillo, S. P. Katikaneni, S. N. Paglieri, B. Solami, *et al.*, *Catalysis Science & Technology* **13**, 2026 (2023).
- ⁶⁴X. Lu, J. Zhang, W.-K. Chen, and A. Roldan, *Nanoscale Advances* **3**, 1624 (2021).
- ⁶⁵A. S. Marfunin, *Advanced mineralogy: volume 1 composition, structure, and properties of mineral matter: concepts, results, and problems*, Vol. 1 (Springer Science & Business Media, 2012).
- ⁶⁶A. Erlebach, H.-D. Kurland, J. Grabow, F. A. Müller, and M. Sierka, *Nanoscale* **7**, 2960 (2015).
- ⁶⁷X. Mou, B. S. Zhang, Y. Li, L. Yao, X. Wei, D. S. Su, and W. Shen, *Angewandte Chemie International Edition* **51**, 2989 (2012).
- ⁶⁸R. Yun, F. Zhan, N. Li, B. Zhang, W. Ma, L. Hong, T. Sheng, L. Du, B. Zheng, and S. Liu, *ACS Applied Materials & Interfaces* **12**, 34122 (2020).
- ⁶⁹H. Tüysüz, F. Schüth, L. Zhi, K. Müllen, and M. Comotti, *ChemCatChem* **7**, 1453 (2015).
- ⁷⁰M. Hattori, N. Okuyama, H. Kurosawa, and M. Hara, *Journal of the American Chemical Society* **145**, 7888 (2023).
- ⁷¹C. Ling, Y. Zhang, Q. Li, X. Bai, L. Shi, and J. Wang, *Journal of the American Chemical Society* **141**, 18264 (2019).
- ⁷²H. Yuzawa, T. Mori, H. Itoh, and H. Yoshida, *The Journal of Physical Chemistry C* **116**, 4126 (2012).
- ⁷³G. Chen, J. Qu, P. Cheah, D. Cao, Y. Zhao, and Y. Xiang, *Industrial & Engineering Chemistry Research* **61**, 11436 (2022).

Supporting Information for
"Theoretical design of nanocatalysts based on $(\text{Fe}_2\text{O}_3)_n$ clusters for
hydrogen production from ammonia"

Sapajan Ibragimov,^{1,2} Andrey Lyalin,^{3,4} Sonu Kumar,⁵ Yuriko Ono,⁵ Tetsuya Taketsugu,^{3,5} and Maciej Bobrowski²

¹*Faculty of Chemistry, Gdańsk University of Technology, Narutowi za 11/12, 80-233, Gdańsk, Poland*

²*Faculty of Technical Physics and Applied Mathematics, Gdańsk University of Technology, Narutowicza 11/12, 80-233 Gdańsk, Poland*

³*Department of Chemistry, Faculty of Science, Hokkaido University, Sapporo 060-0810, Japan*

⁴*Research Center for Energy and Environmental Materials (GREEN), National Institute for Materials Science, Namiki 1-1, Tsukuba 305-0044, Japan*

⁵*Institute for Chemical Reaction Design and Discovery (WPI-ICReDD), Hokkaido University, Sapporo 001-0021, Japan*

(*Author to whom correspondence should be addressed: lyalin@icredd.hokudai.ac.jp)

(Dated: 29 September 2024)

TABLE S1: B3LYP/6-31+G* relative energies calculated with respect to the lowest energy state of kite-like Fe_2O_3

Spin	ΔE (kcal/mol)
0	0.62
4	0.0
5	4.75

The binding energy E_b per unit n of a $(\text{Fe}_2\text{O}_3)_n$ cluster is defined as follows:

$$E_b = -\frac{E_{\text{el}}((\text{Fe}_2\text{O}_3)_n) + E_{\text{ZPE}}((\text{Fe}_2\text{O}_3)_n) - [2nE(\text{Fe}) + 3nE(\text{O})]}{n} \quad (1)$$

where $E_{\text{el}}((\text{Fe}_2\text{O}_3)_n)$ and $E_{\text{ZPE}}((\text{Fe}_2\text{O}_3)_n)$ are the electronic and zero-point energies of a cluster $(\text{Fe}_2\text{O}_3)_n$ with a number of units n , while $E(\text{Fe})$ and $E(\text{O})$ are the energies of free Fe and O atoms.

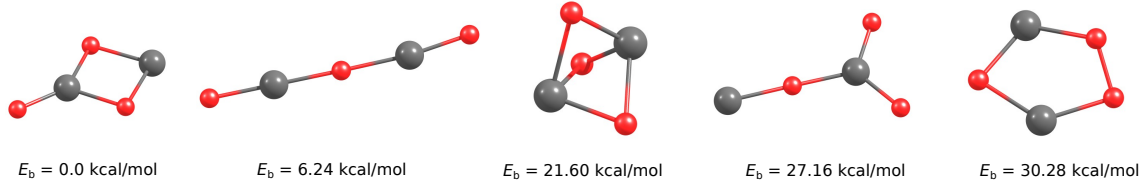


FIG. S1: Five the most stable isomers of Fe_2O_3 with total spin $S=4$. The binding energies, E_b , are shown in inserts.

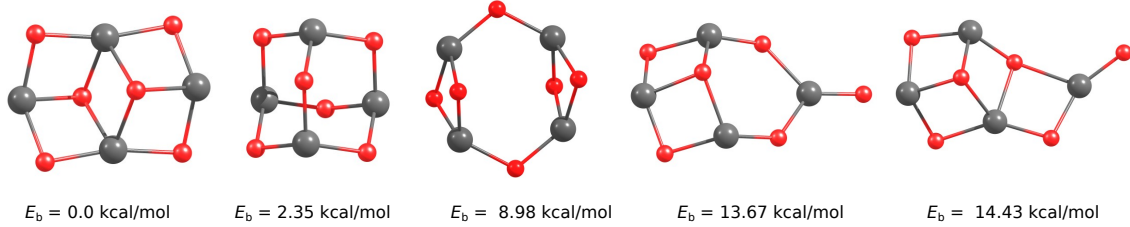


FIG. S2: Five the most stable isomers of $(\text{Fe}_2\text{O}_3)_2$ with total spin $S=10$. The binding energies, E_b , are shown in inserts.

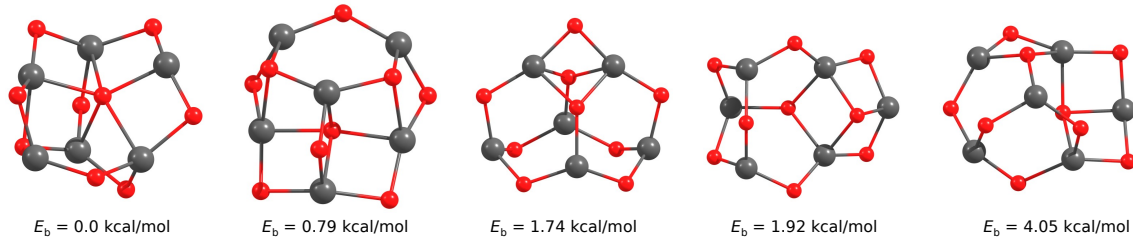


FIG. S3: Five the most stable isomers of $(\text{Fe}_2\text{O}_3)_3$ with total spin $S=15$. The binding energies, E_b , are shown in inserts.

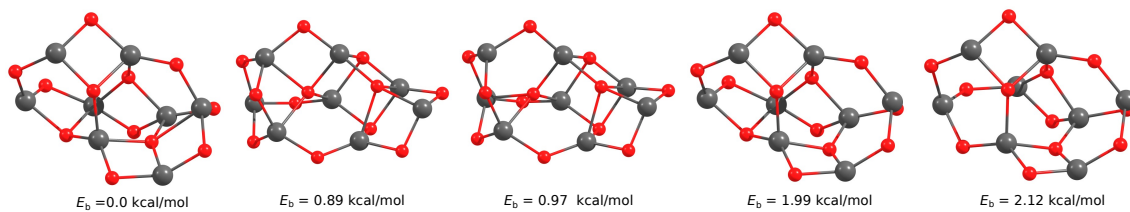


FIG. S4: Five the most stable isomers of $(\text{Fe}_2\text{O}_3)_4$ with total spin $S=20$. The binding energies, E_b , are shown in inserts.

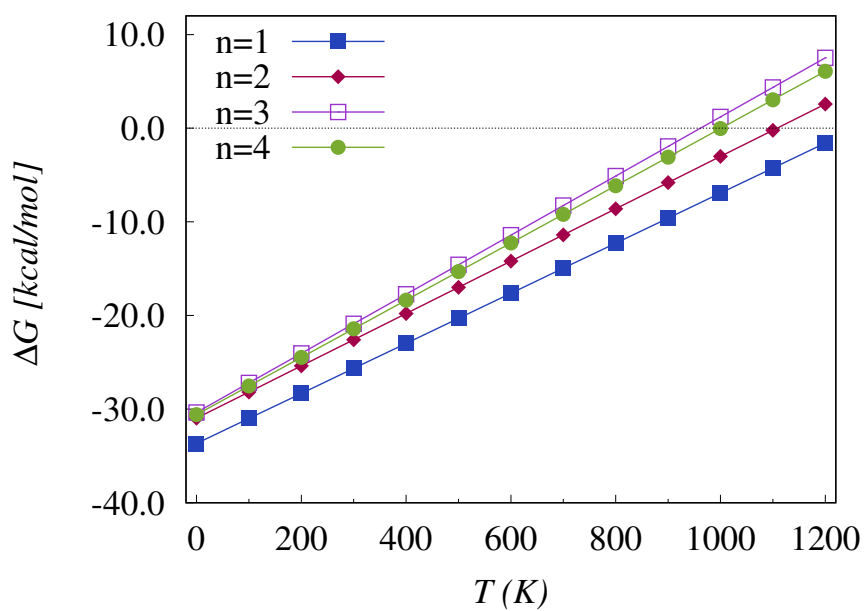
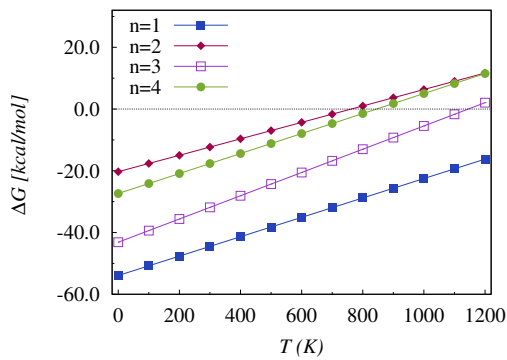
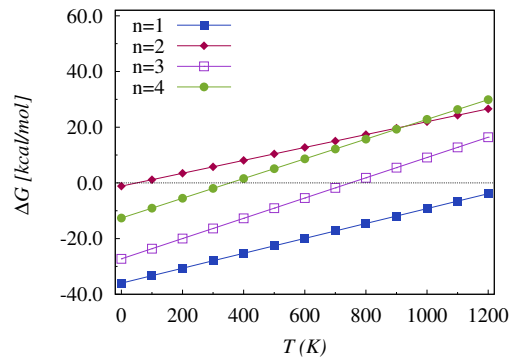


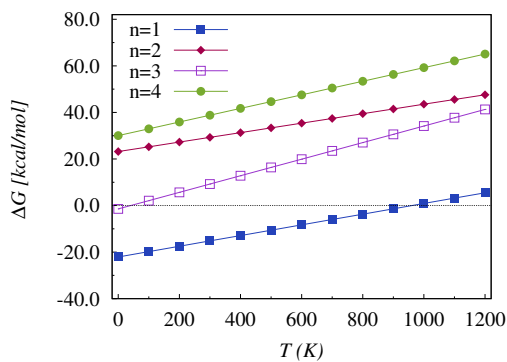
FIG. S5: The temperature dependence of adsorption free energy for NH_3 adsorption on $(\text{Fe}_2\text{O}_3)_n$ $n=1-4$ at 1 atm.



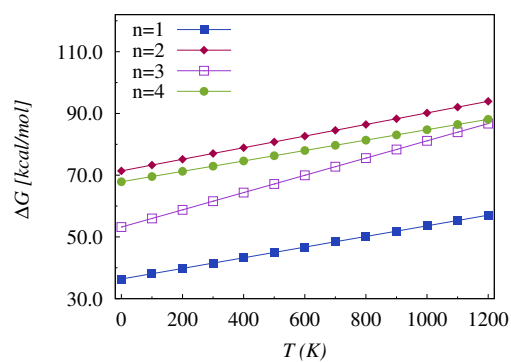
(a) $\text{NH}_3^* + * = \text{NH}_2^* + \text{H}^{**}$



(b) $\text{NH}_2^* + * = \text{NH}^* + 2\text{H}^{**}$



(c) $\text{NH}^* + * = \text{N}^* + 3\text{H}^{**}$



(d) $\text{NH}^* + * = \text{NH}^* + \text{H}_2$

FIG. S6: Variation of Gibbs free energy (ΔG) with temperature for each dehydrogenation step of NH_3 on $(\text{Fe}_2\text{O}_3)_n$ ($n=1-4$) clusters, along with the H_2 formation reactions $\text{NH}^* + 2\text{H}^* = \text{NH}^* + \text{H}_2$ and $\text{N}^* + 3\text{H}^* = \text{N}^* + \text{H}^* + \text{H}_2$.